# PROTEUS

## A Physically Realistic Contrast-Enhanced Ultrasound Simulator—Part II: Imaging Applications

Heiles, Baptiste; Blanken, Nathan; Kuliesh, Alina; Versluis, Michel; Jain, Kartik; Lajoinie, Guillaume; Maresca, David

**DOI**
10.1109/TUFFC.2025.3566437

**Publication date**
2025

**Document Version**
Final published version

**Published in**
IEEE Transactions on Ultrasonics, Ferroelectrics, and Frequency Control

**Citation (APA)**
Heiles, B., Blanken, N., Kuliesh, A., Versluis, M., Jain, K., Lajoinie, G., & Maresca, D. (2025). PROTEUS: A Physically Realistic Contrast-Enhanced Ultrasound Simulator—Part II: Imaging Applications. *IEEE Transactions on Ultrasonics, Ferroelectrics, and Frequency Control*, *72*(7), 866-878. https://doi.org/10.1109/TUFFC.2025.3566437

# PROTEUS: A Physically Realistic Contrast-Enhanced Ultrasound Simulator—Part II: Imaging Applications

Baptiste Heiles, Nathan Blanken, Alina Kuliesh, Michel Versluis, *Member, IEEE*, Kartik Jain,
Guillaume Lajoinie, *Member, IEEE*, and David Maresca

***Abstract*—The development of new imaging paradigms in the field of contrast-enhanced ultrasound (CEUS) is hindered by the difficulty to control complex experimental variables in a laboratory setting, such as vascular geometries, nonlinear ultrasound wave propagation in tissue, or microbubble positions within vessels as a function of time. This development would greatly benefit from the ability to control and reproduce independently these conditions in a simulated environment. Here, we report a physically realistic CEUS simulator, PROTEUS, that generates synthetic contrast-enhanced radio frequency (RF) data. In this article, we show that PROTEUS enables flexible investigations of imaging parameters on CEUS, including innovative transducer architecture, such as row–column addressed arrays, microbubble size distribution, pulse sequences, and vascular geometry. We demonstrate how PROTEUS can emulate various 2-D and 3-D imaging modes, such as pulse inversion (PI) or amplitude modulation (AM), echo particle image velocimetry (PIV), or ultrasound localization microscopy (ULM). Finally, in an investigative simulation case study, we evaluate the impact of microbubble size distribution on ULM on a simulated set of 15 000 frames. It is released as an open-source tool for the scientific community.**

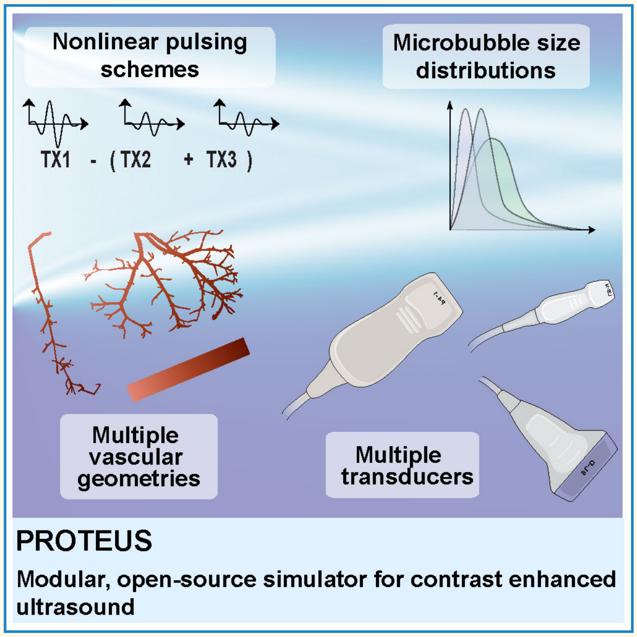

***Index Terms*—Acoustics, blood flow measurement, general physical, ultrasound contrast agents (UCAs), wave propagation.**

Received 21 February 2025; accepted 17 April 2025. Date of publication 12 May 2025; date of current version 1 July 2025. This work was supported by SURFSara through Nederlandse Organisatie voor Wetenschappelijk Onderzoek (NWO) who provided the computing resources on the Dutch national supercomputer Snellius through NWO Grants 2019/ENW/00768083 and 2022/ENW/01266133. The work of Baptiste Heiles was supported in part by the 4TU Precision Medicine program supported by High Tech for a Sustainable Future, a framework commissioned by the four technical universities of the Netherlands, and a Marie-Sklodowska Curie Fellowship of the European Union under Grant MIC-101032769. The work of Alina Kuliesh was supported by the Technical University (TU) Delft Artificial Intelligence (AI) Initiative. The work of Guillaume Lajoinie was supported in part by the 4TU Precision Medicine program supported by High Tech for a Sustainable Future, a framework commissioned by the four technical universities of the Netherlands, and in part by European Union [European Research Council (ERC)-2022-Starting Grant (STG) Super FALCON] under Project 101076844. The work of David Maresca was supported by 4TU Precision Medicine program supported by High Tech for a Sustainable Future, a framework commissioned by the four technical universities of the Netherlands through the 4TU Precision Medicine Program. *(Baptiste Heiles, Nathan Blanken, and Alina Kuliesh contributed equally to this work.) (Corresponding authors: Kartik Jain; David Maresca; Guillaume Lajoinie.)*

Please see the Acknowledgment section of this paper for the author affiliations.

Data is available on-line at https://github.com/PROTEUS-SIM/PROTEUS.

Digital Object Identifier 10.1109/TUFFC.2025.3566437

## I. INTRODUCTION

ULTRASOUND plays a major role in clinical practice. It is used as a gold standard screening method in fields such as pre- and perinatal care [1], as a diagnostic tool for cancer patients [2], as a bedside modality in intensive care units [3], and in general as a primary assessment and patient sorting tool. More specifically, ultrasound is a powerful method to assess normal and abnormal blood flow [4], [5] across the cardiovascular space [6]. Many of these flow imaging applications rely on ultrasound contrast agents (UCAs) to enhance the weak scattering of red blood cells. Clinical UCAs consist of polydisperse phospholipid-coated microbubbles with sizes ranging from 1 to 10 μm [7], [8]. These sizes allow microbubbles to flow together with red blood cells throughout the vasculature, including capillary beds. Microbubbles generate contrast in ultrasound imaging by oscillating volumetrically in response to transmitted ultrasound pressure waves. Recent years have witnessed a wave of novel imaging concepts and therapeutic applications that leverage the unique dynamics of UCAs.

***Highlights***

- **PROTEUS enables CEUS case studies exploiting advanced pulse sequences and custom contrast agents.**
- **PROTEUS enables investigating applications in vascular imaging, e.g., through vector flow imaging and ULM.**
- **PROTEUS enables simulating 3-D imaging by means of virtual 2-D arrays.**

Advances in contrast-enhanced ultrasound (CEUS) have mostly followed three research directions. The first involves improving microbubbles themselves, for example, by making them more monodisperse to enhance the overall nonlinear scattering of the suspension [9], [10], [11] or by modifying their shell to make them sensitive to ambient pressure [12], [13] or PH [14]. Further efforts are being made to functionalize the shell [15], [16], [17] to target biomolecules such as endothelial growth factor [18], load therapeutic payloads [19], [20], [21], or turn them into multimodal agents [22], [23]. Recently, nonphospholipid shell agents consisting of genetically encoded gas vesicles [24] have also been developed for molecular imaging [25], [26], biosensors [27], and vascular reporters [28]. The second direction involves imaging strategies that exploit nonlinear microbubble contrast to reveal vascular information. For example, a framework based on cross-propagating plane waves was recently developed to image nonlinear UCAs with higher specificity [29], [30]. Multiplane wave imaging [31] is based on a pulse sequence that enables CEUS with a higher contrast at the cost of a reduced frame rate [32]. Particle image velocimetry (PIV) analysis of CEUS data enables vector flow imaging (also referred to as echoPIV) [4], [33], [34], [35]. Frequency mixing was proposed as an alternative way to exploit bubble nonlinearity [36]. The use of the highly specific bubble ultraharmonics has also been used for angiography [37]. These strategies can also involve sequence acquisition associated with advanced processing, such as nonlinear singular value decomposition (SVD) [38]. The third direction involves combining the separation and localization of individual UCAs to break the diffraction limit in vascular imaging. By localizing individual microbubbles in the circulation, and reducing their point spread function by an order of magnitude, ultrasound localization microscopy (ULM) is able to resolve targets down to a 10-µm resolution in two [39] and three dimensions [40], [41], [42], [43], [44], [45]. The first clinical ULM demonstrations in humans include transcranial imaging of the cerebral vasculature or transthoracic imaging of intramyocardial coronary arteries [46], [47]. Research efforts are ongoing to develop algorithms that can improve microbubble localization accuracy and decrease ULM acquisition time [48], [49], [50], [51], [52] and to explore the new opportunities offered by ULM for, e.g., functional brain imaging [53], neonatal imaging [54], or stroke assessment [55].

The development of CEUS imaging techniques through experimentation requires significant time and resources. Obtaining an unbiased evaluation of the performance in vivo is often challenging due to the absence of a ground truth. Therefore, there is an urgent requirement for precise simulation tools that can accurately capture the dynamics of blood flow, the acoustic behavior of tissue, and the behavior of microbubbles. These tools are essential for comparing and evaluating new ultrasound flow imaging techniques. Additionally, the effectiveness of machine learning-based methods heavily depends on the availability of authentic training data, which is currently lacking.

In Part I of this article, we introduced PROTEUS, a physically realistic CEUS simulator consisting of four interconnected modules that capture the physics of CEUS imaging. The first module computes blood flow in segmented vascular geometries with a lattice Boltzmann flow solver [56], [57]. The second module propagates microbubbles along the streamlines of this flow. The third module employs the wave propagation toolbox k-Wave to simulate transducer arrays, ultrasound pulse sequences, and wave propagation [58]. The fourth module evaluates microbubble dynamics through an ordinary differential equation solver [59].

Here, in Part II, we demonstrate the potential of PROTEUS with six imaging case studies. First, we simulate nonlinear ultrasound imaging of microbubbles using established pulse sequences [60]. Second, we simulate a row-column-addressed array to demonstrate the 3-D imaging capabilities of the simulator. Third, we compare nonlinear imaging of polydisperse and monodisperse microbubble suspensions. Fourth, we simulate cascaded waves to show the applicability of the simulator to coded-excitation studies. Fifth, we show how PROTEUS can serve to evaluate the accuracy of echoPIV in a macroscopic flow model. Finally, we present an investigative study exploring the impact of the microbubble size distribution on ULM. In all these applications, the knowledge of microbubble positions and microbubble nonlinear scattering serves as a ground truth to benchmark the performance of imaging strategies and computational imaging algorithms. In summary, PROTEUS creates the possibility to develop and test new imaging methods and computational algorithms in the field of CEUS.

PROTEUS is an open-source MATLAB application with a graphical user interface that is freely available at: https://github.com/PROTEUS-SIM/PROTEUS. For instructions on how to install and use the program, the reader is referred to the documentation in the GitHub repository—https://github.com/PROTEUS-SIM/PROTEUS

## II. METHODS

### A. Overview of the Architecture of PROTEUS

In this section, we present a brief overview of the four modules of the PROTEUS simulator. For more details, refer to Part I of this article.

The first module is responsible for the fluid dynamics simulation and relies on the lattice Boltzmann solver Musubi [56], [57]. This module generates physically realistic flow velocities in vascular geometries. In this first release, PROTEUS

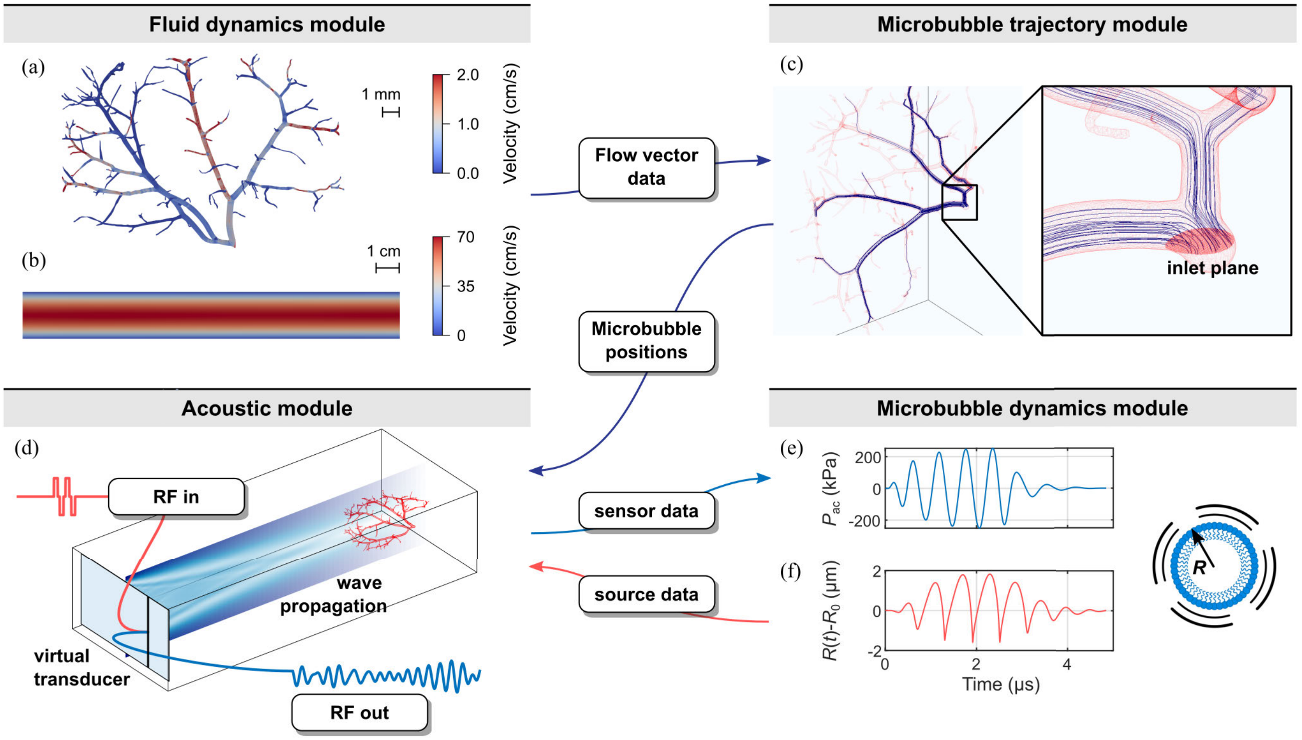

Fig. 1. PROTEUS modules and their connectivity. The data shown here are a compilation of data from Part I of this article and serve to summarize the methodology. The data do not correspond to a full end-to-end simulation with fixed simulation settings. (a) Precomputed fluid dynamics simulations of a rat renal vascular branch. (b) Precomputed fluid dynamics simulations of a macroscopic straight pipe. (c) Intravascular trajectories of individual microbubbles computed by the microbubble trajectory module. (d) Transmit element RF signal, cross section (elevation plane) of a pressure field generated by a virtual phased-array transducer, and a receive element RF signal. (e) Acoustic pressure $P_{ac}$ driving a microbubble. (f) Radial excursion $R(t)$–$R_0$ of the microbubble in response to the driving pressure.

includes three presimulated vascular geometries: a renal vascular branch segmented from an open-source dataset of a rat kidney [61] featuring blood flow velocities up to 11 cm/s, with 90% of the flow below 2.8 cm/s [Fig. 1(a)], a mouse brain arteriole [62] featuring blood flow velocities up to 7 cm/s, with 90% of the flow below 1.6 cm/s, and a 2-cm diameter straight pipe featuring a Poiseuille flow profile with a peak flow velocity of 0.7 m/s [Fig. 1(b)]. Musubi can also process other vascular geometries in STL format and perform direct numerical flow simulations. The computed flow quantities are stored in (visualization toolkit unstructured (VTU) grid [63].

The second module imports the computed flow data and computes the trajectories of all microbubbles embedded in the vascular geometry [Fig. 1(c)]. When a microbubble exits the vasculature at any outlet boundary, a new microbubble is generated at the inlet, based on an inlet density map, and propagated further. This density map ensures a homogeneous distribution of microbubbles throughout all vessels in the geometry.

The third module is in charge of transducer and acoustic wave propagation modeling. We emulate commercially available transducer arrays based on experimental characterization of the impulse response. The wave transmit simulations rely on k-Wave simulations, which are grid-based and support GPU-accelerated computations. The interaction of the transmit wave with the microbubbles and microbubble–microbubble crosstalk (multiple scattering) are simulated by iterative communication between the acoustic module and the microbubble dynamics module. The acoustic simulations in this study were run on an NVIDIA RTX A6000 (48-GB memory) combined with an Intel[1] Core[2] i9-10900KF CPU. We used a phased-array transducer model (P4-1) throughout this study, but any other array with a linear arrangement can be integrated into the acoustic module.

The final module computes the radial response of each microbubble to the incoming ultrasound pressure wave. Three options are provided to model the dynamics of the microbubble shell: the Marmottant model [59], a surface tension curve (surface tension as a function of shell dilation) from high-precision acoustic measurements [64], or a user-defined surface tension curve.

Two computational pipelines are available to simulate the interaction of the transmit wave with the microbubbles and microbubble–microbubble crosstalk (multiple scattering) through iterative communication between the acoustic module and the microbubble dynamics module. The *numerical pipeline* relies entirely on numerical simulations to simulate the wave propagation. The *semi-analytical pipeline* was designed to minimize the computation time and relies on both numerical simulations and analytical solutions to the wave

---

[1] Registered trademark.

[2] Trademarked.

TABLE I
TISSUE PROPERTIES USED IN THIS ARTICLE

| Parameter | Symbol | Value | | Unit |
|---|---|---|---|---|
| | | Tissue | Blood | |
| Density | $\rho_0$ | 1000 | 1060 | kg/m$^3$ |
| Speed of sound | $c_0$ | 1540 | 1584 | m/s |
| Nonlinearity parameter | $B/A$ | 6 | 6 | |
| Attenuation | $\alpha_b$ | 0.75 | 0.14 | dB/MHz$^{1.5}$ |

equation. For more details about the two different implementations, refer to Part I of this article.

PROTEUS allows for arbitrary tissue definition and also provides a list of predefined tissues [65]. In this article, the medium consists of a generic soft tissue in which the vasculature is embedded (see Table I).

## B. CEUS Pulse Sequences

Nonlinear imaging is of primary importance to CEUS imaging. Our first imaging demonstration simulates and compares established CEUS pulse sequences [60]. Specifically,

1) Pulse inversion (PI) is implemented by inverting the pulse of the second transmit, and the nonlinear data is obtained by pulse-to-pulse radio frequency (RF) addition.
2) Amplitude modulation (AM) is implemented using three pulses, in chronological order: a high-amplitude pulse using all elements of the active aperture, a half-amplitude pulse using even elements of the active aperture, and a second half-amplitude pulse using odd elements of the active aperture.
3) Amplitude-modulated PI (AMPI) consists of the same sequence as AM. The only difference being the inversion of the full-amplitude pulse [60].

The propagation medium contains $10^3$ monodisperse microbubbles (2.14-µm radius and 5% polydispersity index) flowing through the renal vascular branch presented in Fig. 1(a). A 2.5-MHz broadband burst of 200 kPa is transmitted with the P4-1 phased-array transducer. Using microbubbles with a radius of 2.14 µm (resonant at about 1.7 MHz) in combination with a broadband transducer (−6 dB at 1.5 and 3.5 MHz) allows for exciting and recording both the fundamental at 1.7 MHz and the second harmonic generated by the microbubbles at 3.4 MHz. The vasculature is embedded in tissue with average acoustic properties (see Table I). The center of the renal vasculature was positioned 6.4 cm below the active surface of the probe to be at the elevation focus of the P4-1 (see Blanken et al. [66]). Unless otherwise specified, all images were reconstructed with a pixel size of $\lambda/5$, and with an image size matching the simulation domain (see Table II). The standard Delay-And-Sum script is provided with the PROTEUS simulator.

## C. 3-D Contrast Imaging

Another possibility offered by PROTEUS is to simulate 2-D arrays to perform 3-D imaging. We modeled a 256-element row–column-addressed array, with a pitch of 200 µm, centered at 6 MHz (−6-dB bandwidth at 3–9 MHz), and transmitted a 2-cycle long pulse at 6 MHz with a pressure amplitude of 200 kPa. This pulse was transmitted using each of the arrays successively to generate a set of 16 angled plane waves, from −7.5° to 7.5° with a regular step size of 1°. The full 128-element aperture was used. A population of 5000 microbubbles with a distribution corresponding to the approved UCA SonoVue[1] (Bracco Suisse SA, Geneva, Switzerland) is seeded in the vasculature, and both the vascular tree and the surrounding tissue are considered to be blood. The RF data are obtained using the semi-analytical pipeline and beamformed using a Delay-And-Sum algorithm. The resulting beamformed volumes are summed to deliver orthogonal plane wave imaging (OPW).

Once RF data are generated with PROTEUS, images are reconstructed using a Delay-And-Sum beamforming algorithm that is provided with PROTEUS and based in part on methodologies published by Perrot et al. [67].

## D. Nonlinear Ultrasound Imaging of Polydisperse and Monodisperse Microbubbles

In the third imaging demonstration, we compare AM ultrasound imaging of two microbubble populations with different size distributions and concentrations. The first population consists of polydisperse microbubbles that emulate the clinically approved UCA SonoVue (Bracco Suisse SA). The distribution was adapted from [68] (for a more detailed description, refer to Part I of this article). The second population consists of monodisperse microbubbles (2.14-µm radius and 5% polydispersity index). The RF element data are generated using the numerical pipeline.

## E. Coded Excitation Schemes

In this fourth demonstration, we use PROTEUS to reproduce the use of coded excitation schemes, and in particular, or cascaded waves [69], [70]. To that end, we simulate the straight pipe, with an in-plane rotation of 15°. We simulate a virtual L12-3 probe with 192 elements, a pitch of 0.2 mm, an elevation focus of 20 mm, and an element length of 5 mm. The −6 dB bandwidth of the transducer was set to 4.5–10 MHz. The transmitted pulse for the plane wave transmission was custom-defined by uploading the one-way transmit waveform of the corresponding transducer as estimated by the Verasonic system. The pulse trains were constructed by repeating these pulses four times with a delay of 1.12 µs, and imparting the polarities as described by Zhang et al. [69]. The tissue consisted of "standard tissue" with a speed of sound of 1540 m/s, a density of 1000 kg/m$^3$, and a B/A coefficient of 6. Tissue inhomogeneity was set to 2%. The vessel was filled with blood, with a speed of sound of 1575 m/s and a density of 1055 kg/m$^3$. The vessel was seeded with 50.000 SonoVue bubbles (of which ∼4.500 were in the simulation volume). A more extensive list of simulation parameters is provided in Table II. The simulation was performed with the hybrid simulator, and the bubbles were "on-grid," owing to the large number of bubbles and the diffraction-limited application. A normally distributed noise with the an arbitrary amplitude

TABLE II
SUMMARY OF THE SIMULATION PARAMETERS USED IN THIS STUDY

| | **Poly- versus monodisperse** | **Pulsing schemes** | **Vector flow imaging** | **ULM** | **Cascaded waves** | **RCA 3D** |
|---|---|---|---|---|---|---|
| Gui parameter files | GUI_param_T51<br>GUI_param_T61<br>GUI_param_T71<br>GUI_param_T81 | GUI_param_T31 to T36 | straight_tube_Re5000_rotation | GUI_param_T1001<br>GUI_param_T1101 | GUI_param_PW<br>GUI_param_CDW_1<br>GUI_param_CDW_2 | GUI_param_RCA (run ”run_RCA.m”) |
| sim. domain (mm) (depth, height, width) | 76.2, 18.4, 30.8 | 76.2, 18.4, 30.8 | 81.2, 18.4, 30.8 | 76.2, 18.4, 30.8 | 37.4, 5.8, 39.3 | 30.5, 30, 30 |
| voxel size (lambda) | 1/8 | 1/8 | 1/8 | 1/8 | 1/5 | 1/5 |
| voxel size ($\mu$m) | 77 | 77 | 77 | 77 | 34.5 | 51 |
| ultrasound frequency | 2.5 | 2.5 | 2.5 | 2.5 | 8.93 | 6 |
| pipeline | numerical | numerical/ semi-analytical | semi-analytical | semi-analytical | semi-analytical | semi-analytical |
| on grid bubbles | no | no | yes | no | yes | yes |
| bubbles per frame | 10 or 1000 | 1000 | 10000 | 15 | 50000 | 5000 |
| bubble type | monodisperse (2.14 um, PDI 5%) or Sonovue | monodisperse (2.14 um, PDI 5%) | monodisperse (2.14 um, PDI 5%) | monodisperse (2.14 um, PDI 5%) or Sonovue | Sonovue | Sonovue |
| tissue inhomogeneity | 2% | 2% | 1% | 2% | 2% | 0% |
| frame rate | 500 | 500 | 1000 | 100 | 8000 | 500 |
| Nunber of frames | 2 | 2 | 500 | 15000 | 20 | 1 |
| probe | P4-1 | P4-1 | P4-1 | P4-1 | custom L12-3 | RC6gV RCA |
| Ncycles | 1 | 1 | 2 | 1 | 4x1 | 2 |
| pressure (kPa) | 200 | 200 | 200 | 200 | 100 | 200 |
| bubble cross-talk (N iter) | 1 | 1 | 0 | 0 | 0 | 0 |
| pulsing scheme | AM | AM, PI, and AMPI | none | AM | none | custom (see methods) |
| inter-pulse-time ($\mu$s) | 100 | 100 | NA | 150 | NA | NA |

of 50 was added to each set of RF lines generated by the simulator. Signals are then decoded using the Delay-And-Sum methodology described in [69] and [71].

### F. Vector Flow Imaging

The fifth imaging demonstration is echo particle image velocimetry (echoPIV), an emerging CEUS imaging application. This technique relies on ultrafast ultrasound to follow the speckle generated by microbubbles in real time, and a velocity field is computed through PIV processing [72]. To model flow in a macroscopic vessel, we simulate $10^4$ monodisperse microbubbles (mean radius 2.14 µm, PDI of 5%) flowing within the 2-cm diameter straight pipe. The pipe is located at a depth of 60 mm from the transducer surface. To simulate a more realistic scenario, the pipe is tilted by applying a 10° rotation in the imaging plane followed by a 15° rotation about the transducer's wave propagation axis. The microbubbles are insonified with the P4-1 transducer transmitting a 200-kPa imaging pulse (approximately 1.5 cycles). The RF lines were simulated using the semi-analytical pipeline, and the images were reconstructed using a Delay-And-Sum beamforming algorithm. Although a simple background subtraction would be sufficient given the static tissue, we apply an SVD filter to the data prior to PIV analysis to respect the standard pipeline. Only the first component is removed. The PIV algorithm consists of a four-path processing with respective kernel sizes of (32 × 32), (32 × 32), (16 × 16), and (16 × 16) pixels. The overlap was set to 75% and the velocity fields are filtered with a Gaussian kernel (3 × 3 pixels).

### G. ULM Processing

The fifth imaging demonstration investigates the impact of microbubble dispersity on ULM. The renal vasculature is embedded in tissue with average acoustic properties. The center of the vascular tree is located at a depth of 64.2 mm with respect to the transducer. Bubbles were insonified with a 2.5-MHz broadband AM pulse sequence of 200 kPa generated by the virtual P4-1 phased-array transducer. The first ULM simulation uses a polydisperse microbubble suspension [68] to emulate the commercial contrast agent SonoVue. The second ULM simulation uses a monodisperse microbubble suspension with a mean radius of 2.14 µm and a polydispersity index of 5%. Both agents are modeled using the experimental surface tension curve [64]. The AM scheme is used to suppress tissue clutter. The RF element data are produced using the semi-analytical pipeline, allowing for rapid generation of 15 000 frames. The RF data are then beamformed on a $\lambda/2$ isotropic grid. Finally, time-invariant speckle patterns are suppressed using a temporal mean filter. The clutter filter is thus based on background subtraction of the average envelope. After the beamforming and filtering steps, the ULM pipeline consists of a standard intensity thresholding method for single microbubble detection. The thresholding parameters are adapted for each one of the distributions to obtain the best possible image and rely on taking a fixed number of the most intense local maxima. After detection, the microbubble positions are inferred using a radial-symmetry algorithm for localization (kernel size of 3 × 3 pixels), and a Kuhn–Munkres pairing assignment algorithm is used for tracking [73]. The tracking step integrates a filter to remove the smallest of the trajectories to improve the final rendering.

## III. RESULTS

### A. CEUS Imaging Simulation

Fig. 2 first shows ultrasound images generated with three common pulse sequences: AM, PI, and AMPI. For comparison, we generated images using both the numerical (left column of Fig. 2) and the semi-analytical pipeline (right column of Fig. 2). Fig. 2(b) displays the B-mode images of

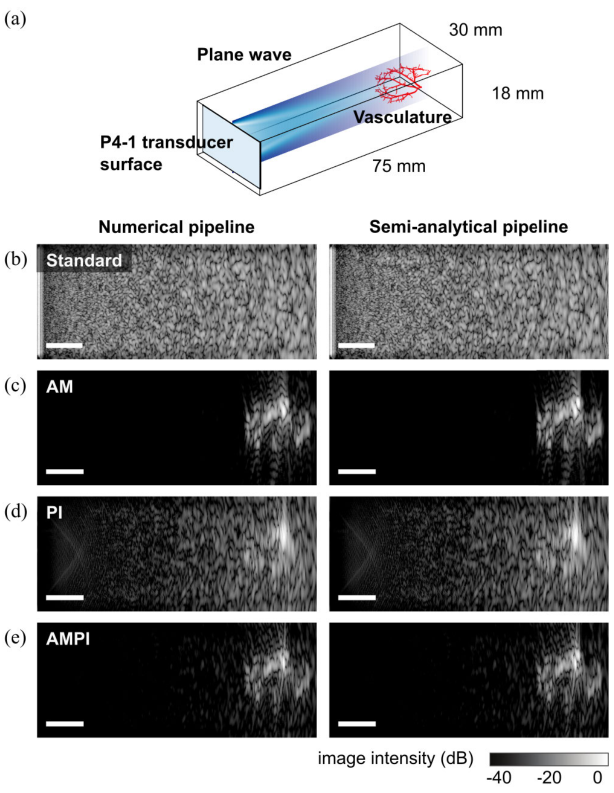

Fig. 2. Nonlinear ultrasound imaging of 1000 resonant microbubbles using conventional pulse sequences. (a) Schematic of the simulation. (b)–(e) Gray-scale ultrasound plane wave images acquired with four different pulsing schemes. (b) Single-pulse plane wave, (c) AM sequence, (d) PI sequence, and (e) AMPI sequence. The left and right images were produced using the *numerical* pipeline and the *semi-analytical* pipeline, respectively. The scale bar represents 1 cm, and the background tissue is given an inhomogeneity of 2%.

the simulated medium and vasculature. The speckle predominantly arises from tissue-mimicking inhomogeneities, and the vascular structure cannot be detected without a pulsing scheme. The B-mode images generated by the numerical and semi-analytical pipelines present similar visual characteristics, with maximum differences in image intensity of 0.8, 1.3, and 0.03 dB for the sets of AM, PI, and AMPI images, respectively. These differences are located in the vessel tree and at the microbubble positions. In the three pulse sequences, tissue signal is observed, because nonlinear ultrasound propagation generates harmonic components that are scattered by the tissue. The speckle pattern, dynamic range, and pulse-related artifacts are similar for both computational pipelines.

The AM images reveal microbubbles in the renal vascular branch with a 40-dB contrast-to-tissue ratio (CTR), while PI and AMPI imaging provide a 20- and 32-dB CTR, respectively. Overall, the simulated results confirm that, even at low acoustic pressure, PI and AMPI contain tissue signal arising from ultrasound wave propagation [60], which makes these modes less specific and thus reduces their dynamic range compared with AM.

## B. 3-D Contrast Imaging

Fig. 3 showcases the capabilities of PROTEUS for 3-D imaging. The renal vasculature [see Fig. 3(a)] was insonified by $16 + 16$ plane waves emitted from a row-column-addressed array to deliver OPW. The vasculature (centered at a depth around 15 mm) was filled with 5000 microbubbles and immersed in a scatter-free medium (more details are provided in Section II). The resulting volume is displayed in Fig. 3(b). The vasculature is clearly visible, as well as pronounced sidelobes, which are expected for such a low number of plane waves. In Fig. 3(c) and (d), the side views of the volumes are presented with an orthographic view. The vasculature is clearly filled with a great number of microbubbles and shows good contrast compatible with CEUS.

## C. Nonlinear Ultrasound Imaging of Polydisperse and Monodisperse Microbubbles

Fig. 4 shows results obtained with an AM pulse sequence for polydisperse and monodisperse populations of 10 (left column) and 1000 microbubbles (right column). Spatial distributions of microbubbles were kept random, as shown in Fig. 3(a). Fig. 4(a) and (d) provides the true locations of the microbubbles. In the B-mode images, the monodisperse microbubbles seem to provide a better mapping of the renal vascular tree than the polydisperse microbubbles. The CTR increases by up to 11 dB for polydisperse microbubbles and up to 18 dB for monodisperse microbubbles, confirming experimental observations [74]. Looking at the results obtained with only ten microbubbles (left column), we can see that in the polydisperse case, only a handful of microbubbles are actually visible in the B-mode which will decrease the fidelity of the vasculature mapping.

Similar to what was observed in the previous case study, nonlinear residual tissue signals that originate from nonlinear wave propagation become significant for low microbubble counts and reduce the CTR [Fig. 4(a) and (b)].

## D. Coded Excitation Schemes

The dual-polarity cascaded waves scheme [69] was designed to increase the SNR of ultrasound images by transmitting two pulse trains that are subsequently decoded using a series of summations, subtractions, and translations on the element RF data, in the time domain. Fig. 5(a) and (b) shows the pulses transmitted by a virtual L12-3 probe for plane wave imaging and dual-polarity cascaded wave imaging, respectively. Dual polarity cascaded waves require two pulse trains. The first train contains one inverted pulse in the fourth position, and the second pulse train contains one inverted pulse in the second position. Fig. 5(c) and (d) shows the resulting B-mode image for plane wave imaging, and cascaded waves imaging, respectively, showing that cascaded wave imaging can be reproduced using PROTEUS, and that is does significantly increases the signal-to-noise ratio of the image, i.e., expectedly, by $10\log_{10}(N) \approx 6$ dB for $N = 4$ pulses per train [70].

## E. Vector Flow Imaging

In Fig. 6(a), we show a conventional B-mode ultrasound image of the simulated pipe embedded in tissue reconstructed with Delay-And-Sum beamforming. We then apply a spatiotemporal clutter filter [75] [Fig. 6(b)] to remove tissue

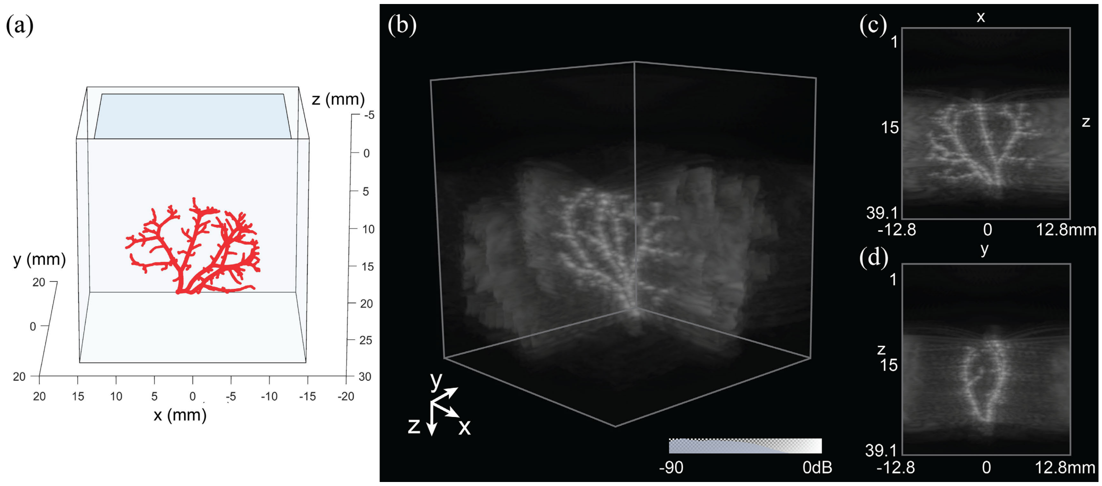

Fig. 3. (a) Schematic of the RCA simulation. (b) OPW of the vasculature using 16 + 16 angles. (c) and (d) Orthogonal cross sections of the vasculature imaged with OPW.

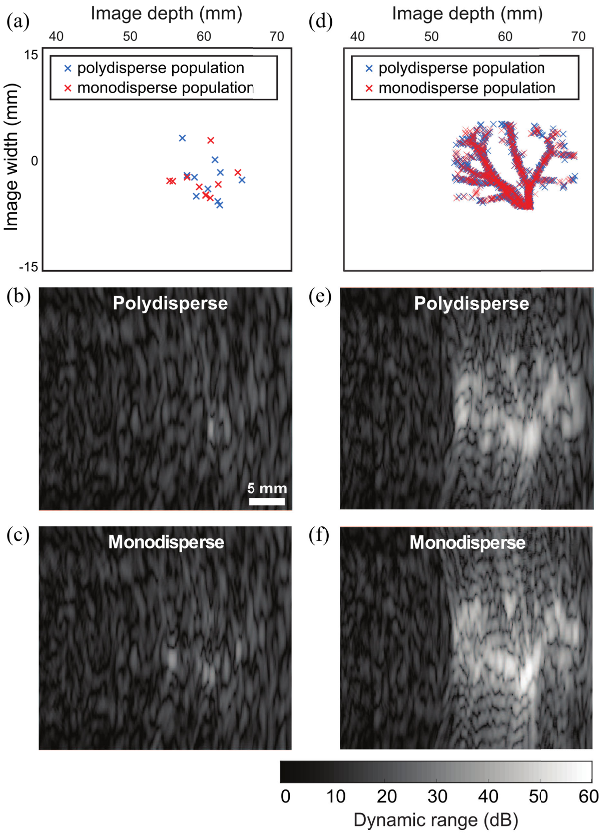

Fig. 4. AM ultrasound imaging of polydisperse and monodisperse microbubbles. (a) Ground-truth location of microbubbles in the rat renal vascular branch for the ten-microbubble cases. (b) AM images of ten polydisperse microbubbles. (c) AM images of ten monodisperse microbubbles. (d) Ground truth location of microbubbles in the rat renal vascular branch for the 1000 microbubble cases. (e) AM images of 1000 polydisperse microbubbles. (f) AM images of 1000 monodisperse microbubbles. The background tissue was created with 2% of inhomogeneity.

signal. As the tissue is stationary in this simulation, tissue speckle remained identical frame after frame and was fully contained in the first principal component of the SVD. The result of a PIV analysis using a state-of-the-art algorithm [76], [77] is shown in Fig. 6(c).

To directly compare with the result of echoPIV, the high-resolution CFD data was spatially resampled to match the resolution of the PIV analysis, and the ground-truth velocity field is displayed in Fig. 6(d). Since the pipe is inclined at an angle in both the imaging plane and about the transducer axis, the vessel walls appear curved.

The difference in velocity between the simulated ground truth and the PIV analysis is shown in Fig. 6(e). We confirm that echoPIV underestimates the velocity by about 7% in the vessel lumen, as was recently claimed in a simplified linear simulation [78]. Moreover, echoPIV overestimates the velocity near the vessel wall, where it predicts a velocity of 0.2 m/s while the ground truth velocity is 0 [78]. Since the resolution of ultrasound is physically limited by its wavelength, any feature smaller than that cannot be accurately quantified. This is also the case close to the vessel wall, where large velocity gradients are present. From a dimensional point of view, velocity profiles in echoPIV can only be resolved accurately if $(\nabla|\vec{v}|\lambda/|\vec{v}|) \ll 1$, i.e., if the relative velocity change over the scale of one wavelength is small as compared to the local velocity magnitude. Here, $\vec{v}$ is the local velocity vector, $\lambda$ is the wavelength, and $|\vec{v}|$ is the velocity magnitude. Furthermore, echoPIV is convolution-based, which makes this condition more stringent since averaging now occurs over the size of the kernel, i.e., $(\nabla|\vec{v}|K/|\vec{v}|) \ll 1$, where $K$ (in m) is the size of the convolution kernel. This quantification further underlines the difficulty to recover wall shear stress with echoPIV. Since wall shear stress is a prime target interest for medical diagnosis, PROTEUS is a valuable tool to develop new and/or dedicated echoPIV strategies and thus improve the accuracy of echoPIV in general.

### F. Effect of Microbubble Size Distribution on ULM

Here, we report an investigation of the impact of microbubble distribution on ULM. Such a comparative study would be

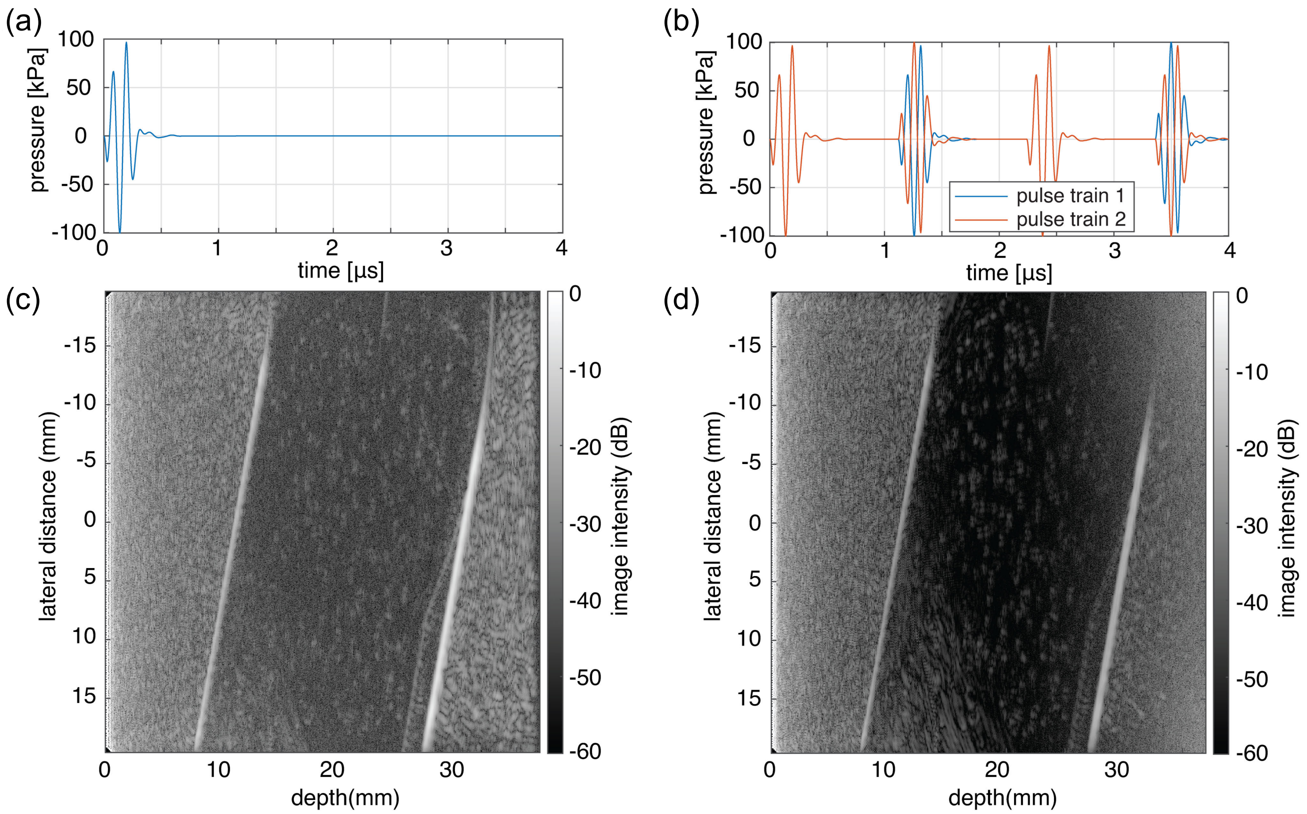

Fig. 5. Cascaded wave imaging. Pulses transmitted by a virtual L12-3 probe for (a) plane wave imaging and (b) cascaded wave imaging. Dual polarity cascaded waves require two pulse trains, each with an inverted pulse. (c) Resulting B-mode image using plane wave imaging. (d) Resulting B-mode image using cascaded waves.

a challenging experiment and demands resources that are not widely available.

To generate ULM images, PROTEUS was used to simulate 15 000 frames acquired at a frame rate of 100 Hz, with each frame capturing 15 microbubbles. Microbubble localization was performed on AM images. AM was chosen to minimize the complexity of necessary tissue and speckle filters and to show the effect of polydispersity.

We adapted the detection threshold to yield the best image possible in each case and found that with polydisperse microbubbles, only three microbubbles on average could be detected beyond which noisy detection became prominent. However, we could reach 15 detections for the monodisperse microbubbles case (see Fig. 7). Polydisperse microbubbles did not enable a complete mapping of the renal vascular tree [Fig. 7(c)]. The vasculature is well-traveled in both cases. However, off-resonance microbubbles are more difficult to detect with AM imaging. As a result, compared to the monodisperse case, several branches are missing, and the density of trajectories per vessel was lower by 49%. There are 25 nodes and 29 branches in the ground-truth vascular tree, and we could successfully identify 13 nodes and 13 branches in the monodisperse case, but only four nodes and five branches in the polydisperse case. For comparison, power Doppler images of both microbubble suspensions are shown in Fig. 7(e).

Velocimetry results [Fig. 7(d)] did not reveal major visible differences between polydisperse and monodisperse contrast agents and in both cases, the velocity measured was in good agreement with the simulated input from the flow dynamics module. Note, however, that in both distributions, some branches of the vasculature are enlarged and branches close together (a separation on the order of one wavelength) become indistinguishable. These results are in agreement with the results of Section III-C as power Doppler images of the monodisperse contrast agent reveal a more exhaustive mapping of the renal vasculature. Nonlinear imaging schemes will only detect the microbubbles emitting strong nonlinear signals. Therefore, the effective concentration of microbubbles usable for ULM in nonlinear schemes is much lower for polydisperse agents, which mechanically increases the required ULM acquisition time. Since we identify 15 and 3 microbubbles per frame in the monodisperse and polydisperse case, respectively, we expect the acquisition time to be increased by as much as 67% in the polydisperse case according to the model from Hingot et al. [79]. Alternatively, this also means that using a nonlinear imaging scheme and a monodisperse microbubble concentration would, for the same acquisition time, result in a threefold increase in microvascular coverage.

## IV. DISCUSSION

### A. Results Summary

We have demonstrated that PROTEUS can generate physically realistic CEUS RF data to investigate a wide range of imaging applications in both 2-D and 3-D. We performed side-by-side comparisons of ultrasound pulse sequences for

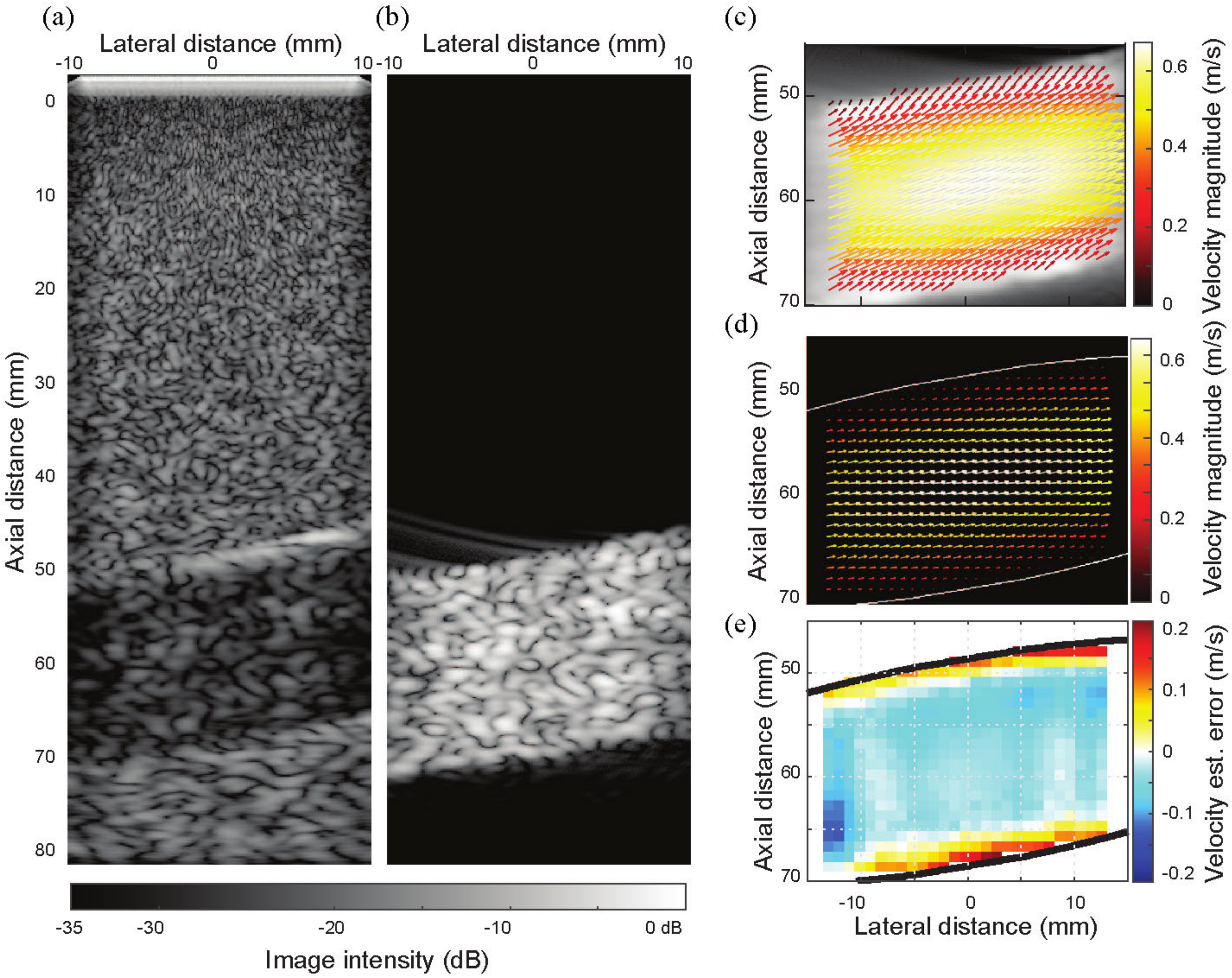

Fig. 6. Ultrasound vector flow imaging simulation. (a) Simulation of a parabolic flow in a 20-mm diameter pipe at a Reynolds number of 5000. The pipe contains 10 000 microbubbles. (b) 500 frames are simulated, and filtered using SVD to suppress the tissue signal. (c) Mean velocity extracted from a PIV analysis of the SVD-filtered image sequence. (d) Ground-truth velocity from the CFD simulation, at the image reconstruction plane. (e) Difference between the velocity estimated from PIV and ground truth.

nonlinear imaging of microbubbles, simulated 3-D contrast imaging, evaluated the echogenicity of resonant microbubble suspensions in AM ultrasound imaging, simulated cascaded waves, quantified the accuracy of echoPIV, and conducted a ULM case study to explore the potential benefit of using monodisperse microbubbles for ultrasound super-resolution. Results about the specificity of AM over PI and AMPI, performance of monodisperse microbubbles in CEUS, and the limitations of echoPIV were in good agreement with previously published experimental observations. Finally, PROTEUS enabled the first investigation of the impact of microbubble dispersity on ULM.

### B. Steady Flow and Tissue

Arguably, the main limitation of this first version of PROTEUS is the lack of time dependency in the tissue scatter and flow. Although these aspects are beyond the current scope, they are important to increase the realism of the simulator and will be a focus for upcoming versions of PROTEUS.

Tissue motion is a well-known source of clutter in ultrasound imaging and processing. The absence of tissue motion makes clutter filtering, e.g., for ULM or echoPIV processing, far simpler than it is in practice, where more advanced postprocessing is required, such as spatiotemporal or complex frequency filters. The temporal mean filtering we implemented already suppresses all noise, and the microbubbles are recovered with very high contrast, since the tissue speckle is identical from one frame to the next. Tissue motion can be implemented in several ways. The most straightforward implementation consists of applying a deformation field to the k-Wave medium, which would come with a large increase of computational cost: for each frame, a deformation field would have to be computed and applied, before recomputing the full wave propagation with the acoustic module. A more efficient way to mimic tissue motion would consist of applying a direct deformation field to a point cloud representation of the medium.

In all of our simulations, we have chosen time-invariant inlet conditions for flow. However, in most vascular flows, there are temporal variations due to the intrinsic nature of cardiovascular activity. Although pulsatile flow can be neglected in arterioles and venules, it is an essential feature of blood flow in larger arteries.

Beyond increasing the time needed to run the CFD simulations, pulsatile flow does not present major difficulties

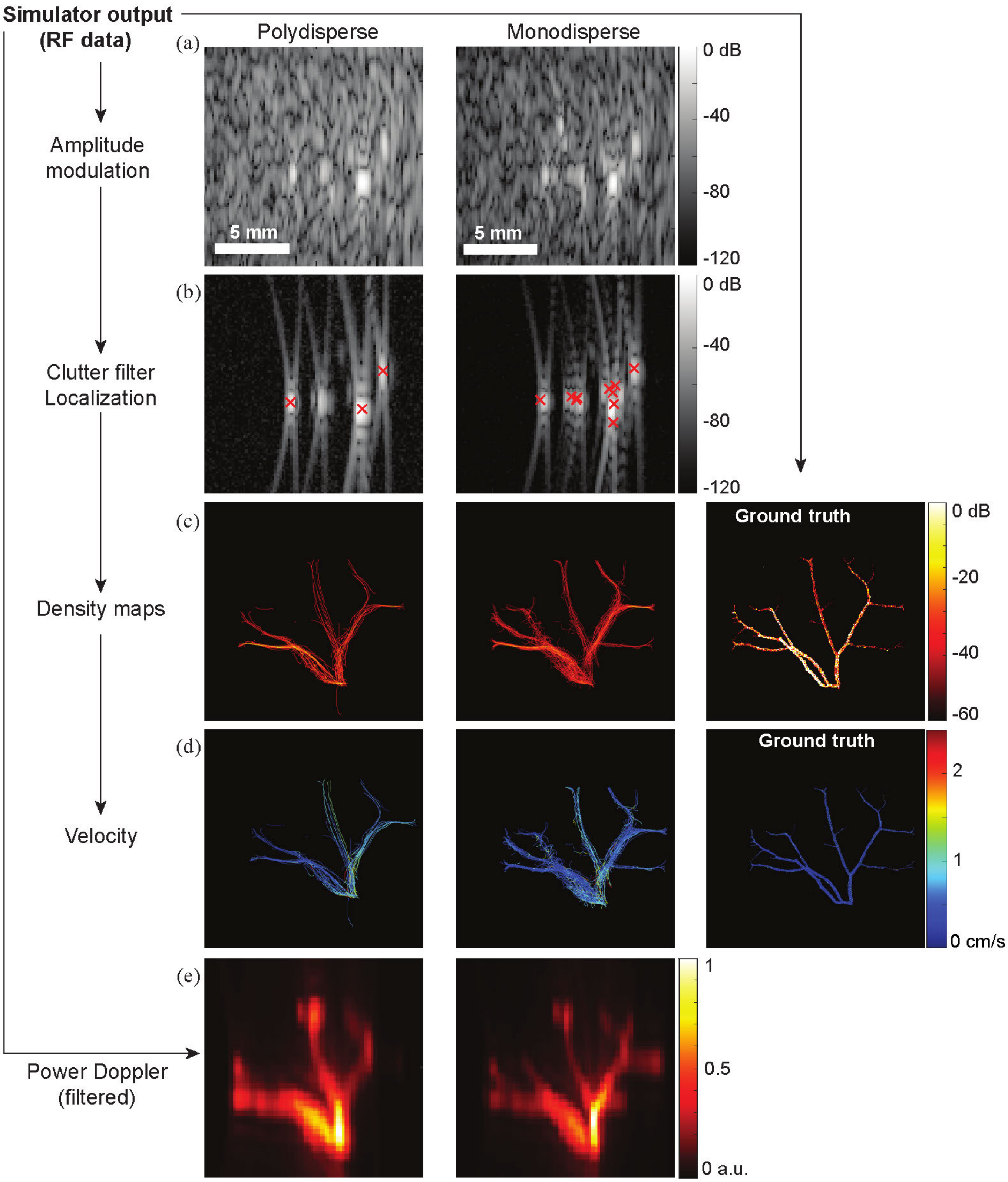

Fig. 7. Influence of microbubble size distribution on ULM. (a) Simulated grayscale images from the rat renal vasculature, which contains 15 monodisperse (left column) or polydisperse (middle column) microbubbles. (b) Filtered grayscale images and microbubble localizations. (c) Density maps created from 15 000 frames (frame rate: 100 Hz). In the right column, all the streamlines used to propagate the microbubbles are shown. (d) Corresponding velocity maps. The ground truth for (c) and (d) is directly provided by the simulator and represents the local speed of each streamline along which the microbubbles are propagated. (e) Power Doppler maps computed from the simulated filtered beamformed RF signals.

within the proposed architecture. The LBM solver can simulate pulsatile flow through time-dependent inlet and/or outlet conditions. The trajectories of microbubbles through the vascular structures then need to be integrated in a time-dependent velocity field.

Finally, pulsatility in major arteries can deform the vessel walls. Accounting for vessel deformation would require both the capability to handle tissue motion and a CFD framework that supports fluid–structure interactions.

### C. Accuracy of the Tissue Scattering

Tissue scatter changes for each tissue type and, in theory, varies as a function of frequency, although the latter is typically neglected. In the case studies presented, we did not quantify the scatter strength of soft tissue but rather programmed a level of inhomogeneity that resulted in a realistic level of tissue speckle in the reconstructed images. However, PROTEUS allows users to reach a higher level of complexity by setting their own tissue properties. This simulated scattering strength also, a priori, depends on the voxel size, which must also be taken into account.

Future development will comprise a more detailed, experimentally derived, representation of various tissue types. This will also pave the road toward representing more complex anatomical features.

### D. Effect of Microbubble Size Distribution on ULM

As a final demonstration of the potential of PROTEUS, we conducted an investigative study comparing ULM based on a monodisperse UCA to ULM based on a conventional polydisperse UCA. Polydisperse microbubbles, excited by high ultrasound frequencies, behave as (nearly) linear scatterers. PROTEUS is by no means limited to this specific aspect of ULM, and could provide quantitative answers on the effect of bubble concentration, pulse sequences depending on flow speed, or the most efficient filters for microbubble detection. This case study allows us to reach several interesting results about the simulator and the effects of microbubble size distribution on ULM. In particular, due to the limited duration of the simulated image sequence, not all the branches are recovered, which is an inherent limitation of ULM. Recovering the whole (accessible) vasculature requires a longer simulation time [79]. Yet, the monodisperse distribution recovers a larger portion of the renal vascular tree, suggesting that monodisperse bubbles could decrease the required acquisition times.

One way to remedy this would be to increase the detection threshold and thus decrease the number of microbubbles in each frame. This may be an option for monodisperse bubbles since they offer a good coverage of the entire vasculature. The cost, however, is a need for more frames to recover all branches. In the polydisperse case, the detection threshold already has to be quite low. Decreasing it even further would lead to a dramatic decrease in image quality. These features are common difficulties encountered in in vivo, and we are confident that PROTEUS is an appropriate platform to investigate, understand, and solve these issues.

Third, we have demonstrated that nonlinear imaging schemes allow for detecting microbubbles without complex filtering. In nonlinear imaging, the resonance of microbubbles plays an important role as resonance increases their scattering cross section. Having more resonant microbubbles increases our capability to isolate them from tissue and increases the number of microbubbles detected. This, in turn, leads to an increase in localization rate and thus a decrease in required acquisition time. PROTEUS allows us to precisely simulate the effect of microbubble distribution, nonlinear imaging schemes, and nonlinear wave propagation independently of each other.

## V. CONCLUSION

We have developed PROTEUS, a physically realistic and versatile open-source simulator that enables numerical investigations of existing and emerging methods in the field of CEUS imaging. PROTEUS greatly facilitates comparative studies and benchmarks that would be experimentally challenging and costly. For methods such as vector flow imaging (or echoPIV), PROTEUS can accelerate the development of more accurate approaches. In the field of ULM, it provides scientists with a tool to generate data and train machine learning-based computational imaging methods. The capabilities of PROTEUS go beyond the examples reported here and will lead to a wave of imaging innovations.

## ACKNOWLEDGMENT

The authors would like to thank Jason Voorneveld for helping with the particle image velocimetry (PIV) analysis. Kartik Jain, David Maresca, and Guillaume Lajoinie jointly supervised this work.

Baptiste Heiles, Alina Kuliesh, and David Maresca are with the Department of Imaging Physics, Delft University of Technology, 2628 CD Delft, The Netherlands (e-mail: d.maresca@tudelft.nl).

Nathan Blanken, Michel Versluis, and Guillaume Lajoinie are with the Physics of Fluids Group, Faculty of Science and Technology and Technical Medical (TechMed) Centre, University of Twente, 7522 NB Enschede, The Netherlands (e-mail: g.p.r.lajoinie@utwente.nl).

Kartik Jain is with the Department of Thermal and Fluid Engineering, Faculty of Engineering Technology, University of Twente, 7522 NB Enschede, The Netherlands (e-mail: k.jain@utwente.nl).

## REFERENCES

[1] L. R. Freud and L. L. Simpson, “Fetal cardiac screening: 1st trimester and beyond,” *Prenatal Diagnosis*, vol. 44, nos. 6–7, pp. 679–687, Apr. 2024.

[2] X.-W. Liang, Y.-Y. Cai, J.-S. Yu, J.-Y. Liao, and Z.-Y. Chen, “Update on thyroid ultrasound: A narrative review from diagnostic criteria to artificial intelligence techniques,” *Chin. Med. J.*, vol. 132, no. 16, pp. 1974–1982, Aug. 2019.

[3] K. Guevarra and Y. Greenstein, “Ultrasonography in the critical care unit,” *Current Cardiology Rep.*, vol. 22, no. 11, Sep. 2020, Art. no. 145.

[4] J. A. Jensen, S. I. Nikolov, A. C. H. Yu, and D. Garcia, “Ultrasound vector flow imaging—Part I: Sequential systems,” *IEEE Trans. Ultrason., Ferroelectr., Freq. Control*, vol. 63, no. 11, pp. 1704–1721, Nov. 2016.

[5] A. A. Oglat, M. Z. Matjafri, N. Suardi, M. A. Oqlat, M. A. Abdelrahman, and A. A. Oqlat, “A review of medical Doppler ultrasonography of blood flow in general and especially in common carotid artery,” *J. Med. Ultrasound*, vol. 26, no. 1, pp. 3–13, Jan. 2018.

[6] I. Aly et al., “Cardiac ultrasound: An anatomical and clinical review,” *Translational Res. Anatomy*, vol. 22, Jan. 2021, Art. no. 100083.

[7] P. Frinking, T. Segers, Y. Luan, and F. Tranquart, “Three decades of ultrasound contrast agents: A review of the past, present and future improvements,” *Ultrasound Med. Biol.*, vol. 46, no. 4, pp. 892–908, Apr. 2020.

[8] E. Stride et al., "Microbubble agents: New directions," *Ultrasound Med. Biol.*, vol. 46, no. 6, pp. 1326–1343, Jun. 2020.

[9] B. van Elburg, G. Collado-Lara, G.-W. Bruggert, T. Segers, M. Versluis, and G. Lajoinie, "Feedback-controlled microbubble generator producing one million monodisperse bubbles per second," *Rev. Sci. Instrum.*, vol. 92, no. 3, Mar. 2021, Art. no. 035110.

[10] T. Segers, A. Lassus, P. Bussat, E. Gaud, and P. Frinking, "Improved coalescence stability of monodisperse phospholipid-coated microbubbles formed by flow-focusing at elevated temperatures," *Lab Chip*, vol. 19, no. 1, pp. 158–167, 2019.

[11] T. Segers, E. Gaud, G. Casqueiro, A. Lassus, M. Versluis, and P. Frinking, "Foam-free monodisperse lipid-coated ultrasound contrast agent synthesis by flow-focusing through multi-gas-component microbubble stabilization," *Appl. Phys. Lett.*, vol. 116, no. 17, Apr. 2020, Art. no. 173701.

[12] V. G. Halldorsdottir et al., "Subharmonic contrast microbubble signals for noninvasive pressure estimation under static and dynamic flow conditions," *Ultrason. Imag.*, vol. 33, no. 3, pp. 153–164, Jul. 2011.

[13] C. Tremblay-Darveau, R. Williams, and P. N. Burns, "Measuring absolute blood pressure using microbubbles," *Ultrasound Med. Biol.*, vol. 40, no. 4, pp. 775–787, Apr. 2014.

[14] D. Terwiel et al., "Acoustic pH sensor for dynamic ultrasound imaging of cellular acidification," *bioRxiv*, Jan. 2025, doi: 10.1101/2025.01.24.634762.

[15] C. J. Slagle, D. H. Thamm, E. K. Randall, and M. A. Borden, "Click conjugation of cloaked peptide ligands to microbubbles," *Bioconjugate Chem.*, vol. 29, no. 5, pp. 1534–1543, Apr. 2018.

[16] B. Geers, I. Lentacker, N. N. Sanders, J. Demeester, S. Meairs, and S. C. De Smedt, "Self-assembled liposome-loaded microbubbles: The missing link for safe and efficient ultrasound triggered drug-delivery," *J. Controlled Release*, vol. 152, no. 2, pp. 249–256, Jun. 2011.

[17] E. Stride, C. Porter, A. G. Prieto, and Q. Pankhurst, "Enhancement of microbubble mediated gene delivery by simultaneous exposure to ultrasonic and magnetic fields," *Ultrasound Med. Biol.*, vol. 35, no. 5, pp. 861–868, May 2009.

[18] M. Smeenge et al., "First-in-human ultrasound molecular imaging with a VEGFR2-specific ultrasound molecular contrast agent (BR55) in prostate cancer: A safety and feasibility pilot study," *Investigative Radiol.*, vol. 52, no. 7, pp. 419–427, Jul. 2017.

[19] J. Deprez et al., "Evaluation of liposome-loaded microbubbles as a theranostic tool in a murine collagen-induced arthritis model," *Scientia Pharmaceutica*, vol. 90, no. 1, p. 17, Feb. 2022.

[20] S. Snipstad et al., "Ultrasound improves the delivery and therapeutic effect of nanoparticle-stabilized microbubbles in breast cancer xenografts," *Ultrasound Med. Biol.*, vol. 43, no. 11, pp. 2651–2669, Nov. 2017.

[21] R. Suzuki and A. L. Klibanov, "Co-administration of microbubbles and drugs in ultrasound-assisted drug delivery: Comparison with drug-carrying particles," in *Therapeutic Ultrasound*. Cham, Switzerland: Springer, 2016, pp. 205–220.

[22] Z. Meng, X. Zhou, J. She, Y. Zhang, L. Feng, and Z. Liu, "Ultrasound-responsive conversion of microbubbles to nanoparticles to enable background-free in vivo photoacoustic imaging," *Nano Lett.*, vol. 19, no. 11, pp. 8109–8117, Oct. 2019.

[23] C. Crake et al., "Enhancement and passive acoustic mapping of cavitation from fluorescently tagged magnetic resonance-visible magnetic microbubbles in vivo," *Ultrasound Med. Biol.*, vol. 42, no. 12, pp. 3022–3036, Dec. 2016.

[24] S. T. Huber, D. Terwiel, W. H. Evers, D. Maresca, and A. J. Jakobi, "Cryo-EM structure of gas vesicles for buoyancy-controlled motility," *Cell*, vol. 186, no. 5, pp. 975–986, Mar. 2023.

[25] B. Heiles, D. Terwiel, and D. Maresca, "The advent of biomolecular ultrasound imaging," *Neuroscience*, vol. 474, pp. 122–133, Oct. 2021.

[26] R. C. Hurt et al., "Genomically mined acoustic reporter genes for real-time in vivo monitoring of tumors and tumor-homing bacteria," *Nature Biotechnol.*, vol. 41, no. 7, pp. 919–931, Jul. 2023.

[27] A. Lakshmanan et al., "Molecular engineering of acoustic protein nanostructures," *ACS Nano*, vol. 10, no. 8, pp. 7314–7322, Jun. 2016.

[28] D. Maresca et al., "Acoustic biomolecules enhance hemodynamic functional ultrasound imaging of neural activity," *NeuroImage*, vol. 209, Apr. 2020, Art. no. 116467.

[29] D. Maresca, D. P. Sawyer, G. Renaud, A. Lee-Gosselin, and M. G. Shapiro, "Nonlinear X-wave ultrasound imaging of acoustic biomolecules," *Phys. Rev. X*, vol. 8, no. 4, Oct. 2018, Art. no. 041002.

[30] A. Matalliotakis, R. Waasdorp, M. D. Verweij, and D. Maresca, "Impact of wavefront shape on nonlinear ultrasound imaging of monodisperse microbubbles," 2024, *arXiv:2403.01452*, doi: 10.1103/PhysRevApplied.22.034062.

[31] E. Tiran et al., "Multiplane wave imaging increases signal-to-noise ratio in ultrafast ultrasound imaging," *Phys. Med. Biol.*, vol. 60, no. 21, pp. 8549–8566, Nov. 2015.

[32] P. Gong, P. Song, and S. Chen, "Improved contrast-enhanced ultrasound imaging with multiplane-wave imaging," *IEEE Trans. Ultrason., Ferroelectr., Freq. Control*, vol. 65, no. 2, pp. 178–187, Feb. 2018.

[33] S. Engelhard et al., "US velocimetry in participants with aortoiliac occlusive disease," *Radiology*, vol. 301, no. 2, pp. 332–338, Nov. 2021.

[34] A. M. Hoving, J. Voorneveld, J. Mikhal, J. G. Bosch, E. Groot Jebbink, and C. H. Slump, "in vitro performance of echoPIV for assessment of laminar flow profiles in a carotid artery stent," *J. Med. Imag.*, vol. 8, no. 1, Jan. 2021, Art. no. 017001.

[35] J. Brum, M. Bernal, N. Barrere, C. Negreira, and C. Cabeza, "Vortex dynamics and transport phenomena in stenotic aortic models using echo-PIV," *Phys. Med. Biol.*, vol. 66, no. 5, Feb. 2021, Art. no. 055026.

[36] K. T. Karlinsky, M. Bismuth, R. Aronovich, and T. Ilovitsh, "Nonlinear frequency mixing ultrasound imaging of nanoscale contrast agents," *IEEE Trans. Biomed. Eng.*, vol. 71, no. 3, pp. 866–875, Mar. 2024.

[37] I. G. Newsome et al., "Implementation of a novel 288-element dual-frequency array for acoustic angiography: In vitro and in vivo characterization," *IEEE Trans. Ultrason., Ferroelectr., Freq. Control*, vol. 68, no. 8, pp. 2657–2666, Aug. 2021.

[38] G. Zhang et al., "Nonlinear singular value decomposition beamforming for ultrasound imaging of gas vesicles," *bioRxiv*, Oct. 2024, doi: 10.1101/2024.10.14.618186.

[39] C. Errico et al., "Ultrafast ultrasound localization microscopy for deep super-resolution vascular imaging," *Nature*, vol. 527, no. 7579, pp. 499–502, Nov. 2015.

[40] B. Heiles et al., "Ultrafast 3D ultrasound localization microscopy using a 32 × 32 matrix array," *IEEE Trans. Med. Imag.*, vol. 38, no. 9, pp. 2005–2015, Sep. 2019.

[41] A. Chavignon, B. Heiles, V. Hingot, C. Orset, D. Vivien, and O. Couture, "3D transcranial ultrasound localization microscopy in the rat brain with a multiplexed matrix probe," *IEEE Trans. Biomed. Eng.*, vol. 69, no. 7, pp. 2132–2142, Jul. 2022.

[42] U.-W. Lok et al., "Three-dimensional ultrasound localization microscopy with bipartite graph-based microbubble pairing and Kalman-filtering-based tracking on a 256-channel Verasonics ultrasound system with a 32 × 32 matrix array," *J. Med. Biol. Eng.*, vol. 42, no. 6, pp. 767–779, Oct. 2022.

[43] H. Favre, M. Pernot, M. Tanter, and C. Papadacci, "Transcranial 3D ultrasound localization microscopy using a large element matrix array with a multi-lens diffracting layer: An in vitro study," *Phys. Med. Biol.*, vol. 68, no. 7, Mar. 2023, Art. no. 075003.

[44] B. Heiles et al., "Nonlinear sound-sheet microscopy: Imaging opaque organs at the capillary and cellular scale," *Science*, vol. 388, 2025, Art. no. eads1325, doi: 10.1126/science.ads1325.

[45] P. Xing et al., "3D ultrasound localization microscopy of the nonhuman primate brain," *eBioMedicine*, vol. 111, Jan. 2025, Art. no. 105457.

[46] C. Demené et al., "Transcranial ultrafast ultrasound localization microscopy of brain vasculature in patients," *Nature Biomed. Eng.*, vol. 5, no. 3, pp. 219–228, Mar. 2021.

[47] J. Yan et al., "Transthoracic super-resolution ultrasound localisation microscopy of myocardial vasculature in patients," 2023, *arXiv:2303.14003*.

[48] N. Blanken, J. M. Wolterink, H. Delingette, C. Brune, M. Versluis, and G. Lajoinie, "Super-resolved microbubble localization in single-channel ultrasound RF signals using deep learning," *IEEE Trans. Med. Imag.*, vol. 41, no. 9, pp. 2532–2542, Sep. 2022.

[49] J. Kim et al., "Improved ultrasound localization microscopy based on microbubble uncoupling via transmit excitation," *IEEE Trans. Ultrason., Ferroelectr., Freq. Control*, vol. 69, no. 3, pp. 1041–1052, Mar. 2022.

[50] X. Chen, M. R. Lowerison, Z. Dong, N. V. C. Sekaran, D. A. Llano, and P. Song, "Localization free super-resolution microbubble velocimetry using a long short-term memory neural network," *IEEE Trans. Med. Imag.*, vol. 42, no. 8, pp. 2374–2385, Aug. 2023.

[51] A. Leconte et al., "A tracking prior to localization workflow for ultrasound localization microscopy," *IEEE Trans. Med. Imag.*, vol. 44, no. 2, pp. 698–710, Feb. 2025.

[52] C. Hahne, G. Chabouh, O. Couture, and R. Sznitman, "Learning super-resolution ultrasound localization microscopy from radio-frequency data," in *Proc. IEEE Int. Ultrason. Symp. (IUS)*, Sep. 2023, pp. 1–4.

[53] N. Renaudin, C. Demené, A. Dizeux, N. Ialy-Radio, S. Pezet, and M. Tanter, "Functional ultrasound localization microscopy reveals brain-wide neurovascular activity on a microscopic scale," *Nature Methods*, vol. 19, no. 8, pp. 1004–1012, Aug. 2022.

[54] S. Schwarz et al., "Ultrasound super-resolution imaging of neonatal cerebral vascular reorganization," *Adv. Sci.*, vol. 12, no. 12, Mar. 2025, Art. no. 2415235.

[55] A. P. Regensburger et al., "Ultrasound localization microscopy for the assessment of microvascular circulation in ischemic perinatal stroke," *Stroke*, vol. 55, no. 12, pp. e323–e325, Dec. 2024.

[56] H. Klimach, K. Jain, and S. Roller, "End-to-end parallel simulations with APES," in *Parallel Computing: Accelerating Computational Science and Engineering (CSE)*. Amsterdam, The Netherlands: IOS Press, Jan. 2014, pp. 703–711.

[57] M. Hasert et al., "Complex fluid simulations with the parallel tree-based lattice Boltzmann solver Musubi," *J. Comput. Sci.*, vol. 5, no. 5, pp. 784–794, Sep. 2014.

[58] B. E. Treeby and B. T. Cox, "k-Wave: MATLAB toolbox for the simulation and reconstruction of photoacoustic wave fields," *J. Biomed. Opt.*, vol. 15, no. 2, 2010, Art. no. 021314.

[59] P. Marmottant et al., "A model for large amplitude oscillations of coated bubbles accounting for buckling and rupture," *J. Acoust. Soc. Amer.*, vol. 118, no. 6, pp. 3499–3505, Dec. 2005.

[60] M. A. Averkiou, M. F. Bruce, J. E. Powers, P. S. Sheeran, and P. N. Burns, "Imaging methods for ultrasound contrast agents," *Ultrasound Med. Biol.*, vol. 46, no. 3, pp. 498–517, Mar. 2020.

[61] D. A. Nordsletten, S. Blackett, M. D. Bentley, E. L. Ritman, and N. P. Smith, "Structural morphology of renal vasculature," *Amer. J. Physiol.-Heart Circulatory Physiol.*, vol. 291, no. 1, pp. H296–H309, Jul. 2006.

[62] G. Hartung et al., "Mathematical synthesis of the cortical circulation for the whole mouse brain—Part II: Microcirculatory closure," *Microcirculation*, vol. 28, no. 5, Jul. 2021, Art. no. e12687.

[63] W. Schroeder, K. Martin, and B. Lorensen, *The Visualization Toolkit*, 4th ed., Clifton Park, NY, USA: Kitware, 2006.

[64] T. Segers, E. Gaud, M. Versluis, and P. Frinking, "High-precision acoustic measurements of the nonlinear dilatational elasticity of phospholipid coated monodisperse microbubbles," *Soft Matter*, vol. 14, no. 47, pp. 9550–9561, Dec. 2018.

[65] H. Azhari, "Appendix A: Typical acoustic properties of tissues," in *Basics of Biomedical Ultrasound for Engineers*. Hoboken, NJ, USA: Wiley, 2010, pp. 313–314.

[66] N. Blanken et al., "PROTEUS: A physically realistic contrast-enhanced ultrasound simulator—Part I: Numerical methods," *IEEE Trans. Ultrason., Ferroelectr., Freq. Control*, vol. 72, no. 7, pp. 848–865, Jul. 2025.

[67] V. Perrot, M. Polichetti, F. Varray, and D. Garcia, "So you think you can DAS? A viewpoint on delay-and-sum beamforming," *Ultrasonics*, vol. 111, Mar. 2021, Art. no. 106309.

[68] T. Segers, P. Kruizinga, M. P. Kok, G. Lajoinie, N. de Jong, and M. Versluis, "Monodisperse versus polydisperse ultrasound contrast agents: Non-linear response, sensitivity, and deep tissue imaging potential," *Ultrasound Med. Biol.*, vol. 44, no. 7, pp. 1482–1492, Jul. 2018.

[69] Y. Zhang, Y. Guo, and W.-N. Lee, "Ultrafast ultrasound imaging with cascaded dual-polarity waves," *IEEE Trans. Med. Imag.*, vol. 37, no. 4, pp. 906–917, Apr. 2018.

[70] C. Nawijn, "Bubbles and waves for ultrasound imaging and therapy," Ph.D. dissertation, Dept. Phys. Fluids, Fac. Sci. Technol., Univ. Twente, Enschede, The Netherlands, 2024.

[71] C. L. Nawijn et al., "Frequency-domain decoding of cascaded dual-polarity waves for ultrafast ultrasound imaging," *IEEE Trans. Ultrason., Ferroelectr., Freq. Control*, vol. 72, no. 3, pp. 321–337, Mar. 2025.

[72] H. J. Vos et al., "Contrast-enhanced high-frame-rate ultrasound imaging of flow patterns in cardiac chambers and deep vessels," *Ultrasound Med. Biol.*, vol. 46, no. 11, pp. 2875–2890, Nov. 2020.

[73] B. Heiles, A. Chavignon, V. Hingot, P. Lopez, E. Teston, and O. Couture, "Performance benchmarking of microbubble-localization algorithms for ultrasound localization microscopy," *Nature Biomed. Eng.*, vol. 6, no. 5, pp. 605–616, Feb. 2022.

[74] A. Helbert, E. Gaud, T. Segers, C. Botteron, P. Frinking, and V. Jeannot, "Monodisperse versus polydisperse ultrasound contrast agents: In vivo sensitivity and safety in rat and pig," *Ultrasound Med. Biol.*, vol. 46, no. 12, pp. 3339–3352, Dec. 2020.

[75] C. Demené et al., "Spatiotemporal clutter filtering of ultrafast ultrasound data highly increases Doppler and fUltrasound sensitivity," *IEEE Trans. Med. Imag.*, vol. 34, no. 11, pp. 2271–2285, Nov. 2015.

[76] J. Voorneveld et al., "High frame rate ultrasound particle image velocimetry for estimating high velocity flow patterns in the left ventricle," *IEEE Trans. Ultrason., Ferroelectr., Freq. Control*, vol. 65, no. 12, pp. 2222–2232, Dec. 2018.

[77] J. Voorneveld et al., "High-frame-rate contrast-enhanced ultrasound for velocimetry in the human abdominal aorta," *IEEE Trans. Ultrason., Ferroelectr., Freq. Control*, vol. 65, no. 12, pp. 2245–2254, Dec. 2018.

[78] J. Voorneveld and J. G. Bosch, "The effect of spatial velocity gradients on block-matching accuracy for ultrasound velocimetry," *Ultrasound Med. Biol.*, vol. 50, no. 1, pp. 67–76, Jan. 2024.

[79] V. Hingot, C. Errico, B. Heiles, L. Rahal, M. Tanter, and O. Couture, "Microvascular flow dictates the compromise between spatial resolution and acquisition time in ultrasound localization microscopy," *Sci. Rep.*, vol. 9, no. 1, p. 2456, Feb. 2019.